Large eddy simulations of an air-helium buoyant jet in a two vented enclosure: influence of the outlet boundary condition

E. SAIKALI[a,b,c], A. SERGENT[b,d], G. BERNARD-MICHEL[a] and C. TENAUD[b]

a. CEA Saclay - DEN/DANS/DM2S/STMF/LIEFT, 91191 Gif-sur-Yvette cedex, France
b. LIMSI, CNRS, Université Paris-Saclay, F-91405 Orsay, France
c. IFD, ED391 SMAER, UPMC Paris 06, Sorbonne Universités, F-75006, Paris, France
d. UFR 919 Ingénierie, UPMC Paris 06, Sorbonne Universités, F-75005, Paris, France

Résumé :

Nous présentons les résultats d'une simulation aux grandes échelles (LES) d'un jet d'hélium au sein d'une cavité équipée de deux évents, initialement remplie d'air. La géométrie de la cavité correspond à celle qui a été utilisée lors des expériences réalisées au CEA-Saclay. Elle a été choisie pour permettre une transition laminaire/turbulent intervenant environ au milieu de la hauteur de la cavité. Cette étude porte principalement sur les conditions aux limites qu'il est nécessaire d'imposer aux frontières du domaine de calcul pour qu'elles n'affectent pas le développement du jet et son effet d'entrainement. Nous observons notamment que des conditions de pression constante appliquées directement au droit des évents sous-estiment le débit volumique d'air entrant dans la cavité. En contrepartie, la prise en compte, dans le domaine de calcul, d'une région extérieure à la cavité semble prédire correctement le flux d'air. Les résultats sont ainsi en bon accord avec les données expérimentales obtenues par mesures PIV.

Abstract :

We present numerical results from large eddy simulations (LES) of an air-helium buoyant jet in a two vented enclosure. The geometrical configuration mimics the experimental setup studied at CEA Saclay. The dimension of the enclosure was chosen to ensure a laminar/turbulent transition occurring at about the middle height of the cavity. This study focuses on the influence of the boundary conditions on the jet development and its entrainment behavior. We observe that applying constant pressure outlet boundary conditions directly at the vent surfaces underestimates the volumetric flow rate of air entering the enclosure. On the contrary, modeling an exterior region in the computational domain better predicts the air flow-rate entrance. Results are then in good agreement with the experimental PIV data.

Key words : Buoyant jet, vented enclosure, Air/Helium mixture, Large Eddy Simulations, boundary conditions, CEA TRUST-TrioCFD

1   Introduction

The present work is devoted to security assessment of systems using hydrogen as energy carrier. In such systems, hydrogen gas is stored inside bottles from which it is distributed through pipes. In accidental situations, hydrogen escapes and rises inside the medium in a form of a plume-jet that entrains air and potentially forms a dangerous-flammable mixture. This issue is well presented by Cariteau et al. in [1].

A dimensionless Richardson number (Ri) can be used to characterize and predict the flow regime by comparing buoyant-to-inertial strengths at the leakage position. For high values of Ri compared to unity, a pure plume regime is predicted and the flow can become turbulent due to gravitational accelerations. However, for Ri≪ 1, a pure jet regime is predicted and turbulence originates from the inertial accelerations. The present paper aims at simulating a particular case for a Ri slightly less than unity where the development of a buoyant jet is supposed. In such type of flows, a transition from an inertial-driven jet into a buoyancy-driven plume occurs in a short distance above the leakage position [2].

Following a physical point of view, the problem is considered as an intrusion of a light fluid into a denser one which, under specific conditions, leads to density stratification inside the medium. This subject is encountered in many technical and engineering applications such as fuel leakage in containments, jets entering mixing chambers, smokestack discharge, study of severe accident scenarios, fire modeling and ventilation [3, 4]. In the present work, we consider the medium to be a two vented enclosure. Following a security assessment and since the usage of hydrogen in experiments requires a great caution, a particle image velocimetry (PIV) experiment was carried out at CEA Saclay on a helium-air buoyant jet. The experimental data will be compared to the numerical results.

Being a widely used tool for simulating complex turbulent flows [5], large eddy simulations (LES) have been performed for the present work. The small unresolved scales of motion are modelled by using the classical Smagorinsky sub-grid scale (SGS) model. We consider in this paper the complete three dimensional (3D) Cartesian geometry and no axi-symmetrical assumption is a priori made.

Numerical simulations of buoyant jets in two vented cavities are extremely interesting for several reasons. The buoyant jet configuration is challenging for computational fluid dynamics (CFD) codes as there exists a rapid transition from laminar to turbulence within a short distance above the intrusion position due to the strong buyant forces. In addition, sharp density gradients occur at the jet boundaries that can lead, in the presence of gravity, to Rayleigh-Taylor instabilities [6]. One of the key-points is the treatment of the outlet boundary conditions that becomes more challenging by considering two outlet boundaries. The main issue is the open problem regarding the best outlet boundary conditions that must be applied on the vents to represent the real flow. This paper aims at highlighting the influence of the outlet boundary conditions on the flow by taking into account an additional exterior region in the computational domain, moving the outlet boundary away from the vents. We then expect that this will allow simulations to correctly represent the real flow.

This paper is organized as follows: the model and the numerical methods are discussed in section two. Section three is devoted to the numerical results and the experimental validation. Conclusions and future perspectives are drawn in section four.

2 Model and numerical methods

2.1 Physical and numerical configurations

The physical problem to be studied is the behavior of a leaked light fluid in a two vented enclosure causing the formation of a buoyant jet (figure 1). The experiment that has been carried out at CEA Saclay models the problem by injecting pure helium through a cylindrical pipe with a constant volumetric flow-rate $Q = 5$ Nl/min into a two vented parallelepiped enclosure filled initially with air at rest. All the physical properties of the light helium gas are referred to with the $_{in}$ subscript (meaning "injected"), while the subscript $_{am}$ is used to denote the ambient air. The pipe used for the injection is of diameter $d = 10^{-2}$ m and long enough to assure that a well developed Poiseuille flow is attained. The dimensions of the cavity are $W \times L \times H = 4.9 \times 5 \times 14.9 \times 10^{-6}$ m^3. We note that the height of the configuration H was selected so as to obtain a transitional flow regime from laminar to turbulent, predicted to occur at $H/d \gg 5$ [7]. In addition, the length L and the width W are chosen to take into account the jet spreading angle which is estimated close to 11-12° [8], thus avoiding the interaction of the jet boundary with the lateral walls of the cavity. The two vents are considered to be identical with a surface area $5 \times 2.9 \times 10^{-4}$ m^2 and both located on the right vertical wall. Plexi-glass of thickness 5×10^{-3} m is used for the solid wall boundaries. A schematic representation of the experimental set-up is shown in figure 1.

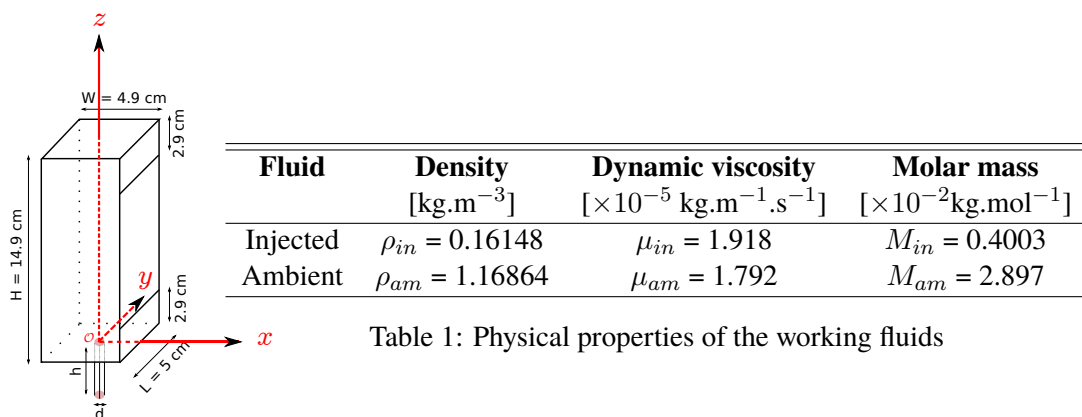| Fluid	Density [kg.m^{-3}]	Dynamic viscosity [$\times 10^{-5}$ kg.m^{-1}.s^{-1}]	Molar mass [$\times 10^{-2}$kg.mol^{-1}]
Injected	$\rho_{in} = 0.16148$	$\mu_{in} = 1.918$	$M_{in} = 0.4003$
Ambient	$\rho_{am} = 1.16864$	$\mu_{am} = 1.792$	$M_{am} = 2.897$

Table 1: Physical properties of the working fluids

Figure 1: Experimental set-up

We assume that the temperature was not varying during the experiment ($T = 25°$ C) and that the thermodynamic pressure p is constant. For simplicity, we consider that $p = 10^5$ Pa ≈ 0.98 atm. Physical properties of the working fluids following the previous assumptions are summarized in table 1.

Characteristics of the desired flow are given in terms of the dimensionless injection Richardson and Reynolds numbers

$$\mathrm{Ri}_{in} = \frac{g(\rho_{am} - \rho_{in})\, d}{\rho_{in} u_{in}^2} \approx 0.14 \quad \text{and} \quad \mathrm{Re}_{in} = \frac{\rho_{in} u_{in}\, d}{\mu_{in}} \approx 180$$

where u_{in} is the maximum velocity at the injection in m.s^{-1}.

The dimensions used in the numerical configuration are the same as those used in the experiment except for the height of the pipe h which is limited to 3×10^{-2} m. We impose a Poiseuille velocity profile at the entrance (bottom) of the pipe to make sure that the velocity distribution along the pipe matches the fully developed steady state solution in the real experiment. We have verified by numerical simulations

with different $h \geq 3 \times 10^{-2}$ m that no impact on the solution was recorded inside the cavity whatever the height h is.

2.2 Governing equations

The flow is governed by the conservation of mass, momentum and scalar species equations coupled with an equation of state for gas mixture, used to determine the mixture density from the species mass fractions [9, 10]. We emphasize that under the justified isothermal and isobar assumptions, it is unnecessary to solve the energy conservation equation. Considering a Mach number Ma = 0.007 and a significant density ratio ($\frac{\rho_{am}}{\rho_{in}} \approx 7.24$), the low Mach number (LMN) approximation is valid [11]. Thus, by asymptotic analysis, the total pressure splits into a sum of a only time dependent thermodynamic pressure $p(t)$ used in the state equation and a space-time dependent hydrodynamic pressure $P(\mathbf{x}, t)$ used in the momentum equation, where $\mathbf{x}$ denotes the space coordinate vector [12].

Applying spatial filtering ($^{-}$) and using density weighted Favre-filtered quantities ($^{\sim}$) with $\tilde{\varphi} = \overline{\rho\varphi}/\overline{\rho}$ for any considered quantity φ, the system of LES governing equations reads [6]

$$\frac{\partial \overline{\rho}\tilde{Y}_1}{\partial t} + \frac{\partial}{\partial x_i}(\overline{\rho}\tilde{u}_i\tilde{Y}_1) = \frac{\partial \overline{\xi}_i}{\partial x_i} + \frac{\partial \overline{\xi}_i^{\text{SGS}}}{\partial x_i}, \tag{1}$$

$$\overline{\rho} = \frac{p\overline{M}}{RT}, \tag{2}$$

$$\frac{\partial \overline{\rho}\tilde{u}_j}{\partial t} + \frac{\partial}{\partial x_i}(\overline{\rho}\tilde{u}_j\tilde{u}_i) = -\frac{\partial \overline{P}}{\partial x_j} + \frac{\partial \overline{\tau}_{ij}}{\partial x_i} + \frac{\partial \overline{\tau}_{ij}^{\text{SGS}}}{\partial x_i} + \overline{\rho}g_j, \tag{3}$$

$$\frac{\partial \overline{\rho}}{\partial t} + \frac{\partial}{\partial x_i}(\overline{\rho}\tilde{u}_i) = 0, \tag{4}$$

where $\overline{\rho}$ is the filtered mixture density, $\tilde{Y}_1$ and $\tilde{Y}_2$ are respectively the helium and air mass fractions, satisfying $\tilde{Y}_1 + \tilde{Y}_2 = 1$, $\tilde{u}_i$ is the mass average component of the velocity vector $\tilde{\mathbf{u}} = (\tilde{u}_1, \tilde{u}_2, \tilde{u}_3)$, $\overline{\xi}_i = \overline{\rho} D \frac{\partial \tilde{Y}_1}{\partial x_i}$ is the molecular diffusion term modeled by Fick's law with a mixture diffusion coefficient $D = 6.91 \times 10^{-5}$ m^2.s^{-1}, $\overline{M} = (\sum_{i=1}^{2} \frac{\tilde{Y}_i}{M_i})^{-1}$ is the mixing molar mass where $M_1 = M_{in}$ and $M_2 = M_{am}$, $R = 8.314$ J.K^{-1}.mol^{-1} is the specific gas constant, $\overline{\tau}_{ij} = 2\mu\overline{e}_{ij}$ is the viscous stress tensor for Newtonian fluids with $\overline{e}_{ij} = \frac{1}{2}(\frac{\partial \tilde{u}_i}{\partial x_j} + \frac{\partial \tilde{u}_j}{\partial x_i}) - \frac{1}{3}\delta_{ij}\frac{\partial \tilde{u}_k}{\partial x_k}$ and μ is the mixture dynamic viscosity calculated as a function of the mass fraction and fluid physical properties as in [9, 13], δ_{ij} the Kronecker symbol and $g_j = (0, 0, -g)$ the gravity vector.

We use the classical Smagorinsky model to close the additional sub-grid scale (SGS) terms appearing in equations (1) and (3). Thus components of the Reynolds stress tensor $\overline{\tau}_{ij}^{\text{SGS}}$ are expressed following:

$$\overline{\tau}_{ij}^{\text{SGS}} = \overline{\rho}(\tilde{u}_i\tilde{u}_j - \widetilde{u_i u_j}) = 2\mu_{\text{SGS}}\overline{e}_{ij}. \tag{5}$$

The SGS dynamic viscosity μ_{SGS} is calculated as

$$\mu_{\text{SGS}} = \overline{\rho}(C_s\Delta)^2\sqrt{2\,\overline{e}_{ij}\overline{e}_{ij}}, \tag{6}$$

where Δ is the filter width taken to be $(\delta_x\delta_y\delta_z)^{1/3}$ and δ_x, δ_y and δ_z are the effective mesh spacing [6, 14].

The unresolved turbulent scalar flux $\overline{\xi}_i^{\text{SGS}}$ is modeled by using a classic Fourier's law as:

$$\overline{\xi}_i^{\text{SGS}} = \overline{\rho}(\tilde{u}_i\tilde{Y}_1 - \widetilde{u_i Y_1}) = \frac{\mu_{\text{SGS}}}{Sc_{\text{SGS}}}\frac{\partial \tilde{Y}_1}{\partial x_i}. \tag{7}$$

The Smagorinsky coefficient C_s and the turbulent Schmidt number Sc_{SGS} are considered constant and uniform throughout the whole domain; 0.18 and 0.7 respectively [15, 16]. In what follows, although denoting filtered quantities, the averaging symbol over the resolved fields is removed for simplicity.

2.3   Post-treatment quantities

We denote by $< \cdot >_t$ the time averaged quantities, calculated for a considered quantity $\varphi(t)$ as

$$< \varphi(t) >_t = \frac{1}{t - t_{\text{start}}} \int_{t_{\text{start}}}^{t} \varphi(t)dt, \tag{8}$$

where t_{start} corresponds to the starting time of the statistical recordings. The volumetric and helium mass flow-rates crossing each vent are calculated respectively as

$$Q_v^i = \int_{\partial\Omega_{out}^i} u_1 d\sigma \quad \text{and} \quad q_{He}^i = \int_{\partial\Omega_{out}^i} \rho_{in} X_1 u_1 d\sigma, \tag{9}$$

where $i = \{bot, top\}$ and $\partial\Omega_{out}^{bot}$, $\partial\Omega_{out}^{top}$ denote the surface area of the bottom and top vent respectively. X_1 is helium volume fraction defined as $X_1 = (\rho - \rho_{am})/(\rho_{in} - \rho_{am})$.

The total mass of helium inside the cavity with volume V is

$$\mathcal{M}_{He} = \int_V \rho_{in} X_1 dV. \tag{10}$$

We denote the kinetic energy by E_k where $2E_k = \sum_i u_i^2$.

2.4   Numerical methods

The system of equations is solved in a sequential way at each time iteration using a semi-implicit scheme, which treats implicitly the diffusion terms and explicitly the convective ones. Thus, the time step δt at each iteration is selected to satisfy the convective Courant-Friedrichs-Lewy condition CFL_{conv} (maximum reached $\delta t_{\text{max}} \approx 4.5 \times 10^{-4}$ s). The discretization employs a Finite Difference Volume (FDV) method on a staggered grid [17]. The spatial discretization for all derivative terms is carried out by a second ordered centered scheme except for the convective term of (1) where a third order quadratic upstream interpolation for convective kinematics (QUICK) scheme is used to ensure the monotonicity property of Y_1. The temporal discretization is performed using a second order Runge-Kutta (RK2) scheme. The linear systems resulting from implicit treatment of the diffusion terms are solved by the conjugate gradient method.

To solve the pressure-velocity problem, an incremental projection method is employed where the variable of the Poisson equation is the pressure increment $\phi = P^{t+\delta t} - P^t$ which is solved by an iterative symmetric successive over relaxation (SSOR) procedure. The pressure increment ϕ is finally used for correcting the velocity field over the domain to satisfy the divergence constraint obtained from equation (4).

At the initial state, the whole cavity is filled with pure air at rest. The boundary conditions are the following: at the inlet boundary $\partial\Omega_{in}$ situated at the bottom end of the cylindrical pipe, a fixed convective mass flux equal to $\rho_{in}Q$ ($Q = 5$ Nl/min) is imposed with flat profiles for $\rho = \rho_{in}$ and $Y_1 = 1$, whereas a parabolic profile is imposed for $\mathbf{u}$. On the wall boundaries $\partial\Omega_w$, a no-slip boundary condition is applied for $\mathbf{u}$ with a homogeneous Neumann condition for all the scalars ρ, Y_1 and P. At the outlet boundaries $\partial\Omega_{out}$, a fixed pressure $P = \rho_{am}gz$ is imposed for a considered height z with a homogeneous Neumann condition for $\mathbf{u}$. A homogeneous Neumann condition is imposed on ρ and Y_1 if $\mathbf{u}.\hat{\eta} \geq 0$; $\hat{\eta}$ is the outward unit normal at the outlet surfaces. Otherwise, the Dirichlet conditions $\rho = \rho_{am}$ and $Y_1 = 0$ are imposed.

2.5 Numerical set-up and validation

Numerical computations have been carried out for four different geometrical configurations labelled from 1 to 4 using the CEA TRUST-TrioCFD code in the MPI parallel version [17]. In configuration 1, the outlet boundary condition is directly prescribed at each vent surface. However, this is not the case for the three other configurations where an exterior domain, of different dimensions, is directly attached to outer vent surfaces and therefore moving the outlet boundary condition away from the cavity. The exterior domain has a horizontal extension Lx, span-wise length $L + (2 \times Ly)$ and a height $H + (2 \times Lz)$. A summary of the considered configurations can be read from table 2. In the present work, we assume that Ly is not varying from configurations 2 to 4 and the effect due to the variation of the horizontal and vertical dimensions is presented.

Configuration	Exterior	Lx [cm]	Ly [cm]	Lz [cm]	Cell numbers	MPI procs
1	No				1,117,204	24
2	Yes	2.6	1.5	1.3	2,163,268	40
3	Yes	4	1.5	2	2,858,668	54
4	Yes	6	1.5	3	4,038,796	80

Table 2: Descriptions of the computational domains.

A uniform cubic cell per block has been used with a cell step size of $\delta = 7 \times 10^{-4}$ m in each direction, compared to an estimated Kolmogorov length scale $\eta = 2.1 \times 10^{-4}$ m ($\delta/\eta = 3.3$) [18]. δ is kept constant whatever the configuration is. The origin of the Cartesian system $\mathcal{O}(0, 0, 0)$ is placed at the top center of the injection pipe. A layer of 5×10^{-3} m width around the vents in configurations 2-4 is imposed with wall boundary condition to account for the plexi-glass thickness in the real experiment. In figure 2, we present a sketch of the different computational domains. Red surfaces indicate the position of $\partial\Omega_w$, $\partial\Omega_{in}$ in yellow and finally the blue surfaces are for $\partial\Omega_{out}$. The grid inside the pipe is identical in the four configurations (subfigure (a)). Subfigure (b) represents the computational domain of configuration 1. Subfigure (c) indicates the $\partial\Omega_w$ of configurations 2 - 4 where a sketch of their complete domain is presented in subfigure (d).

A grid convergence study has been carried out for configuration 1 on seven different uniform meshes of step size decreasing with a geometric factor $q = 1.3$ from 2×10^{-3} m to 4.14×10^{-4} m. The mean values of the helium mass fraction Y_1 and velocity magnitude $|\mathbf{u}|$ show satisfactory converged LES results starting from a grid of step size of 7×10^{-4} m. We note that the convergence on the standard deviation quantities is much slower but satisfactory converged values has however been reached.
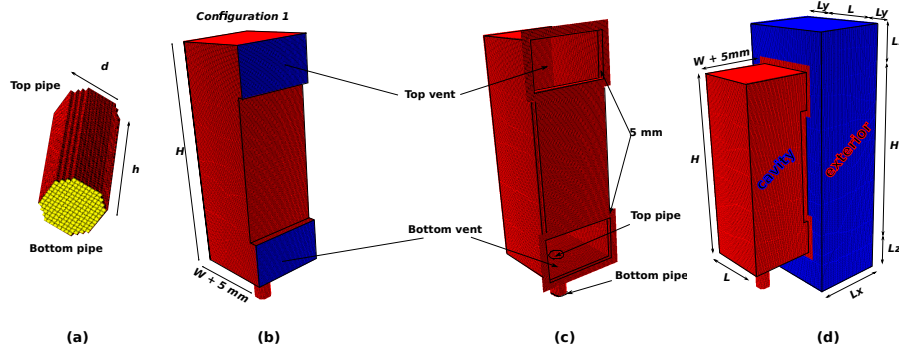
Figure 2: 3D sketch of the computational domains: $\partial\Omega_w$ on red surfaces, $\partial\Omega_{in}$ on yellow surface and $\partial\Omega_{out}$ on blue surfaces.

3   Results

The simulations are carried out over 40 s. of physical time, where a quasi steady state solution is assumed to be reached after approximately the first 4 s. Statistics are recorded starting from $t_{\text{start}} = 5$ s. with a frequency $f_{\text{stat}} = 1/\delta t$ Hz.

3.1   Outlet boundary condition influence

3.1.1   Flow pattern: cavity

In order to study the influence of the outlet boundary conditions on the flow, we consider the four configurations described in section 2.5. We focus on the time-averaged flow pattern: velocity field, helium distribution and global quantities defined by equations (9) and (10) in section 2.3.

First we consider the time averaged kinetic energy distribution $< E_k >_t$ in the vertical mid plane (figure 3).
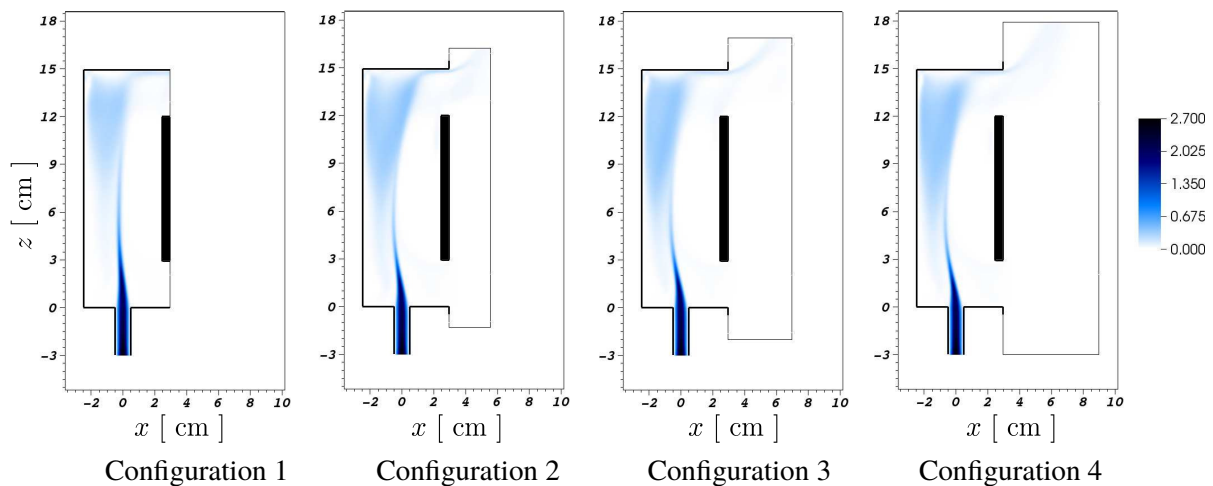
Figure 3: Time averaged flow pattern in the vertical mid xz-plane ($y = 0$) for configurations 1 to 4: kinetic energy iso-contours ($< E_k >_t$ [m^2.s^{-2}]).

We observe that the jet axis is deviated towards the wall facing the vents as a consequence of the inflow from the bottom vent. However, this deviation is more significant when considering an exterior domain (configurations 2 to 4). In all cases, the plume part of the buoyant jet is reoriented from the mid height

towards the vents wall due to the aspiration from the top vent. We note that the kinetic energy is mainly concentrated inside the bottom jet axis and in a more diffuse way at a large part near the wall facing the vents where the buoyancy forces are dominant.

This can be seen in figure 4 which shows the time averaged distribution of the helium volume fraction $< X_1 >_t$ in the same plane. We can note that cavity configurations that take into account an exterior domain contain more helium than configuration 1 in the upper part of the cavity. However, it has been found that configuration 1 contains the maximum helium mass (see table 3) due to the difference in the structure of the jet close to the injection. This is confirmed by the values of the time averaged helium mass flow-rate $< q_{He}^{top} >_t$ at the top vent (table 3), where the smallest helium flow rate leaving from the top vent is seen in configuration 1. Moreover the size of the external domain influences the helium stratification mainly near the top vent, where the air-helium mixture exits the cavity. It seems that outlet boundary condition in the reduced dimension of configuration 2 introduces a blockage of the flow and leads to a more intense horizontal stratification in the exterior domain. The effect is reduced by increasing the depth of the external domain, as seen in configuration 4 of figure 4.
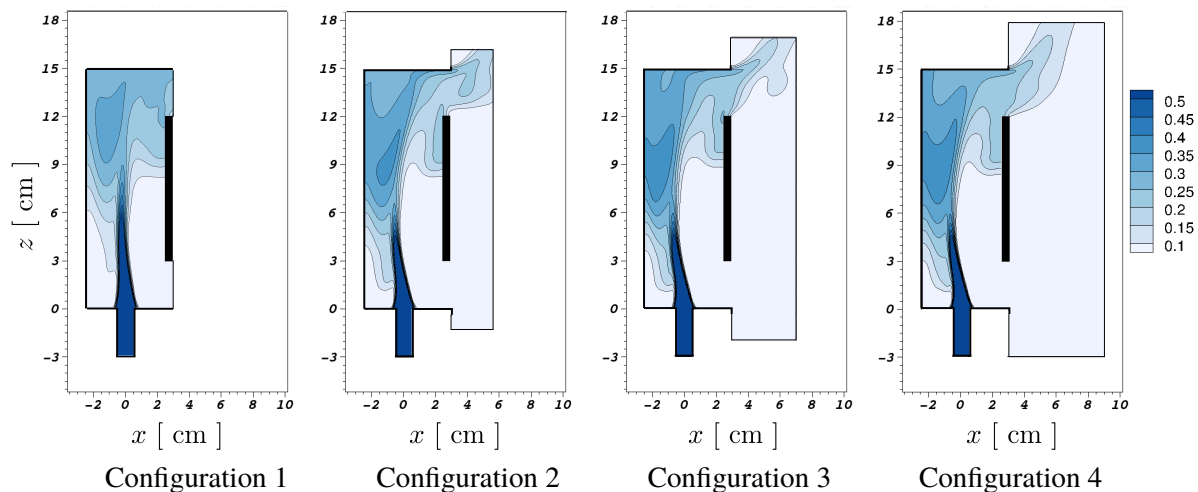

Configuration 1   Configuration 2   Configuration 3   Configuration 4

Figure 4: Time averaged flow pattern in the vertical mid xz-plane ($y = 0$) for configurations 1 to 4: iso-contours of the time average volume fraction $< X_1 >_t$.

Configuration	$< \mathcal{M}_{He} >_t$ [$\times 10^{-6}$ kg]	$< q_{He}^{top} >_t$ [$\times 10^{-5}$ kg.s^{-1}]	$< Q_v^{bot} >_t$ [$\times 10^{-4}$ m^3.s^{-1}]	$< Q_v^{top} >_t$ [$\times 10^{-4}$ m^3.s^{-1}]
1	8.72686	1.419418	-2.579636	3.482771
2	7.95684	1.435510	-2.873982	3.778890
3	8.00131	1.441133	-2.720516	3.623242
4	8.03707	1.437088	-2.812328	3.719466

Table 3: Time averaged Global quantites : helium total mass, mass and volumetric flow-rates.

Only the region containing mainly pure air close to the bottom vent, is unchanged by the modification of the computing domain. A significant influence on the x-horizontal velocity component u_1 is also seen. This is illustrated by the time averaged $< u_1 >_t$ in the vertical mid plane (figure 5). In all configurations we see that, in addition to the helium jet injected from the pipe, pure air enters the cavity from outside through the bottom vent. It impacts the axis of the jet and entrains with helium while rising to dilute an air-helium mixture in the upper part of the cavity. A part of this mixture leaves the cavity through the top vent while the remaining goes into a recirculating motion.
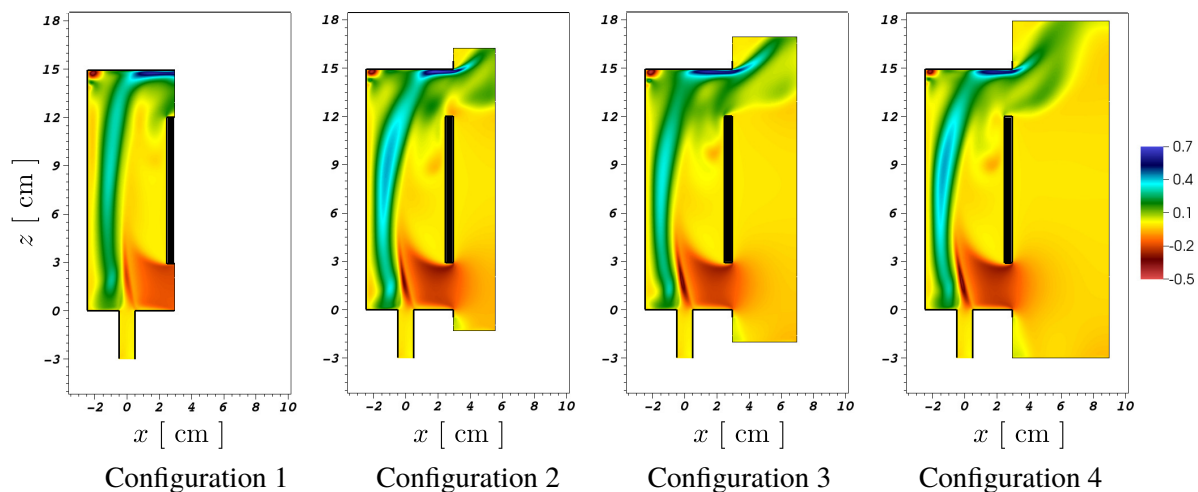
Figure 5: Time averaged flow pattern in the vertical mid xz-plane ($y = 0$) for configurations 1 to 4 : iso-contours of the $< u_1 >_t$ x-horizontal velocity component.

For a global comparison, the time averaged volumetric flow-rates $< Q_v^{bot} >_t$, $< Q_v^{top} >_t$ passing respectively through the bottom and top vents have been calculated and summarized in table 3. We see that configurations with an exterior domain have the highest volumetric flow-rates. Considering a constant injection flow-rate, this result is not surprising as far as the mass of helium in configurations 2 to 4 is less than what has been found in configuration 1. Compared to the injected volumetric flow rate Q, we find a 1% relative error on the species conservation balance. We emphasize that this error is within the numerical error range since the integration was carried out with a first order interpolated values of $< u_1 >_t$ at the vents surfaces.

3.1.2 Flow pattern: bottom vent region

The behavior of the flow at the bottom vent region is influenced by taking an exterior domain into consideration. We see that fresh air enters configuration 1 in almost a uniform way and with absolute velocities smaller than those compared to configurations 2 to 4. The $< u_1 >_t$ velocity profiles in configurations 2 to 4 are almost similar having high absolute values near the edges of the bottom vent, and thus slightly modified with the size of the exterior domain. A description of the flow near the bottom vent with and without an exterior domain is illustrated by streamlines in the vertical mid plane (figure 6).

We study the influence at a horizontal plane crossing the bottom vent (figure 7) where the $< u_1 >_t$ fields look almost the same in all configurations. Fresh air coming with the inflow impacts the jet axis in all the cases. After this impact, the flow spreads symmetrically with respect to the jet axis in two parts. In each part, two opposite vortices are created: one continues to recirculate near the corner of the cavity and the other one circumvents the jet axis until it collides with the one symmetrically coming from the other side of the jet. When these two counter-rotating vortices collide, they form a dipole that accelerates and enters within the jet axis causing a deformation of the initial circular structure. Finally, the dipole is convected upward and an other dipole forms repeating the same mechanism. This behavior can be illustrated by the time averaged velocity stream lines in the same plane (figure 8). The horizontal profiles of $< u_1 >_t$ at the vent surface for all configurations is presented on the same figure. In the
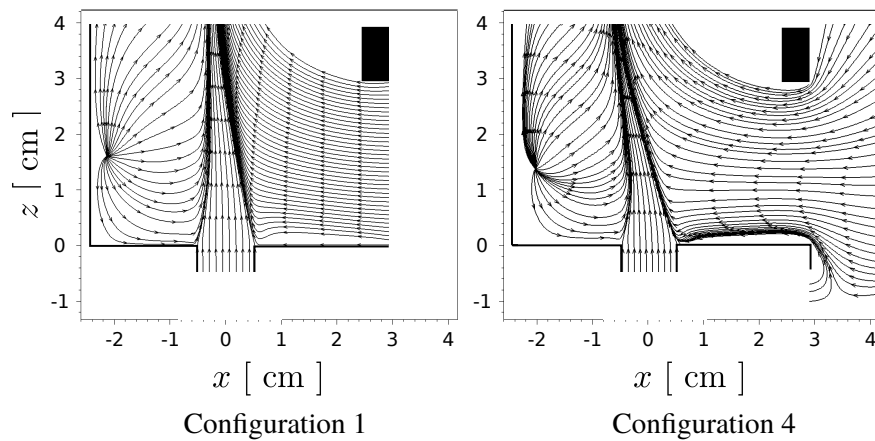
Figure 6: Time averaged flow pattern in the vertical mid xz-plane ($y = 0$) near the bottom vent for configurations 1 to 4 : stream lines of $< \mathbf{u} >_t$.
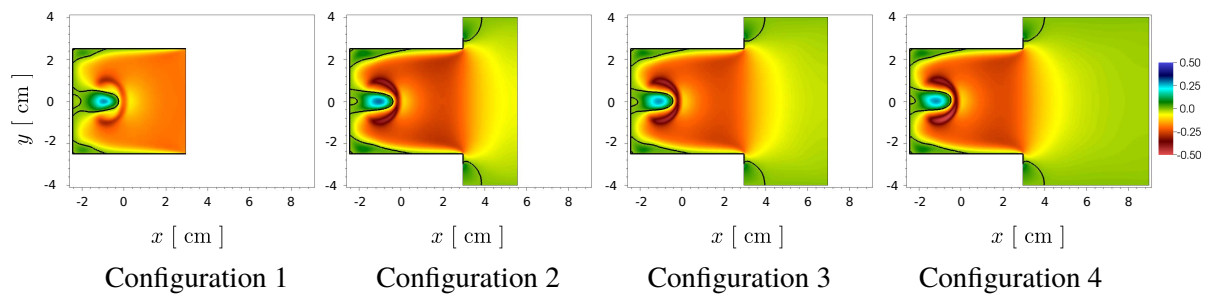

Figure 7: Time averaged flow pattern in the horizontal xy-plane ($z = 2$ cm) for configurations 1 to 4 : iso-contours of the $< u_1 >_t$ x-horizontal velocity component. Zero values are enhanced by a thick black contour.
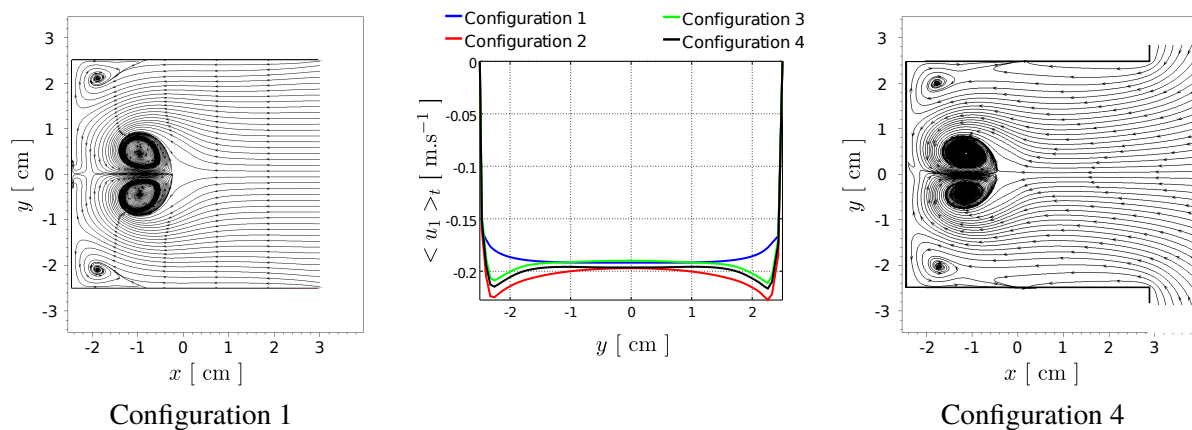

Figure 8: Time averaged flow pattern in the horizontal xy-plane ($z = 2$ cm). Left and right: stream lines of $< \mathbf{u} >_t$ for configurations 1 and 4, middle: $< u_1 >_t$ span-wise profiles of the x-horizontal velocity component for configurations 1 to 4 along the bottom vent's width.

middle part of the vent, a almost uniform velocity is reached in all configurations. However, the values at the edges of the vent are strengthened with configurations that consider an exterior domain.

The influence of the deformation of the jet, initially circular, can be seen in all configurations by plotting the contour of $< X_1 >_t$ at the same horizontal plane (figure 9). A symmetrical distribution
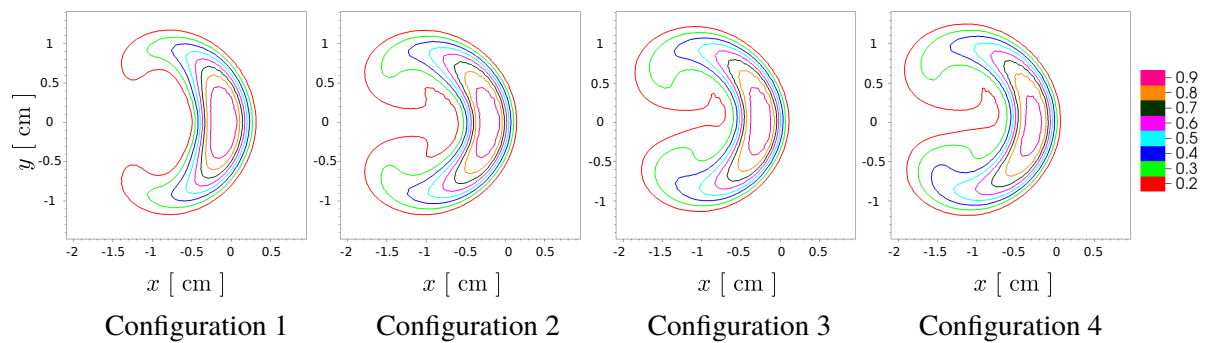
Figure 9: Time averaged flow pattern in the horizontal xy-plane ($z = 2$ cm) for configurations 1 to 4: line contours of the time averaged volume fraction $< X_1 >_t$.

is seen in configurations 1 and 2. The horizontal helium distribution starts losing this symmetry from configuration 3. This loose suggests that a low frequency flapping motion of the jet occurs horizontally in the xy-plane. Identical helium levels are recovered for all cases, although configuration 1 indicates higher capacity of helium compared to configurations 2 to 4. This can be illustrated by comparing the surface area of the line contour corresponding to 90 % of helium.

3.1.3 Flow pattern: top vent region

In all configurations, the mixture leaves the cavity with the highest velocity $< u_1 >_t \approx 0.65$ m.s^{-1} in a top thin layer (recall figure 5). However, the profile of $< u_1 >_t$ in the vertical plane of the top vent depends on the configuration used (figure 10). On the one hand, a symmetrical behavior is observed in configuration 1. On the other hand, taking into account an exterior domain breaks the symmetrical behavior of the outward flow. We claim for such configurations that a "*Coanda effect-like*" takes place where the flow at the top of the cavity sticks to a vertical wall and leaves the domain more intensively from a specific corner. We could easily figure out that a low frequency flapping motion might occur. Further analysis must be undertaken to better understand the dynamics. Although not presented in this paper, we emphasize that the same observation has been detected by considering a finer mesh.

A small inflow from the top vent is seen for configurations 1, 3 and 4 compared to a bigger inflow zone in configuration 2, mainly due to the reduced size of the exterior domain. This comparison can be illustrated by looking at the vertical profiles along the middle of the vent (figure 10 middle). At this specific vertical location, we see that the highest values are given with configuration 1. Nevertheless, a convergence study on the size of the exterior domain is necessary to further analyze in details the flow dynamics.

3.2 Experimental validation

To validate the numerical results and to conclude on the configuration that can be considered as the best in representing the real experiment, we use the available PIV measurements at the bottom region of the cavity in the vertical plane. The vertical profile of the time averaged $< u_1 >_t$ is presented in the vertical plane of the bottom vent (figure 11).

Configuration 1 shows almost a uniform profile which differs to what is obtained by configurations 2 to 4. Almost similar profiles are found whatever the configuration with an exterior domain is considered.
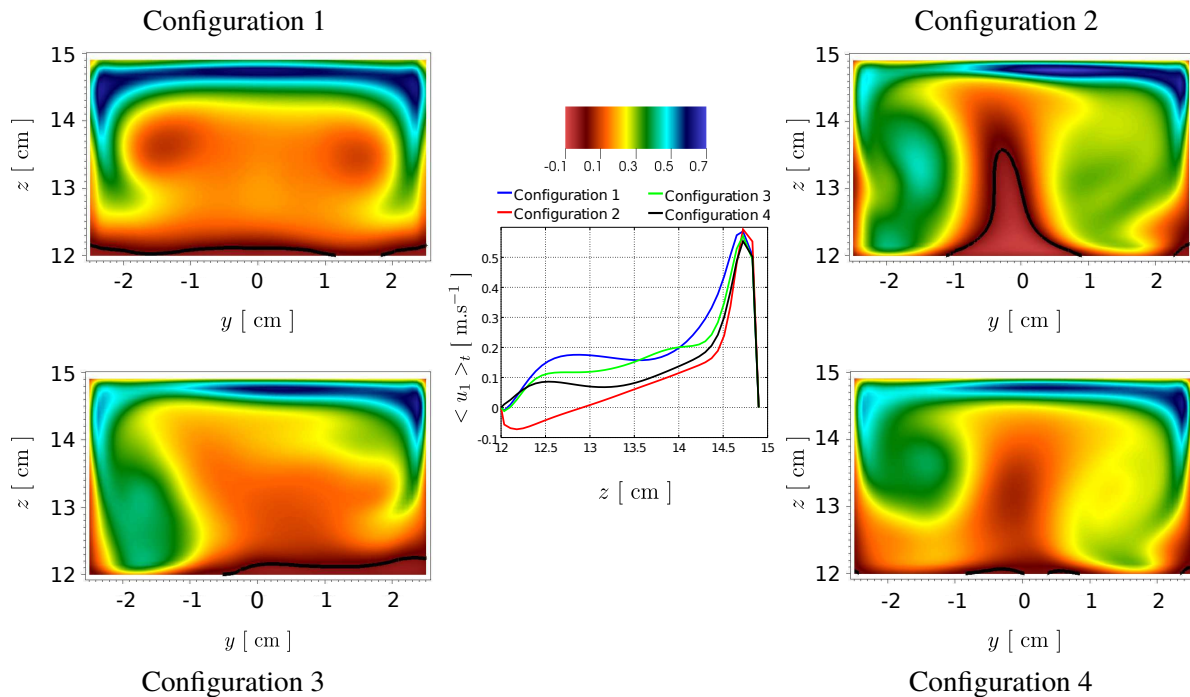
Figure 10: Time averaged flow pattern in the vertical yz-plane ($x = 0.0295$ cm) at the top vent surface for configurations 1 to 4. Left and right: $< u_1 >_t$ x-horizontal velocity component iso-contours, middle: corresponding mid-vertical profile ($y = 0$). Thick black lines of the contour plots denotes the zero contour line indicating the limit of the back flow.
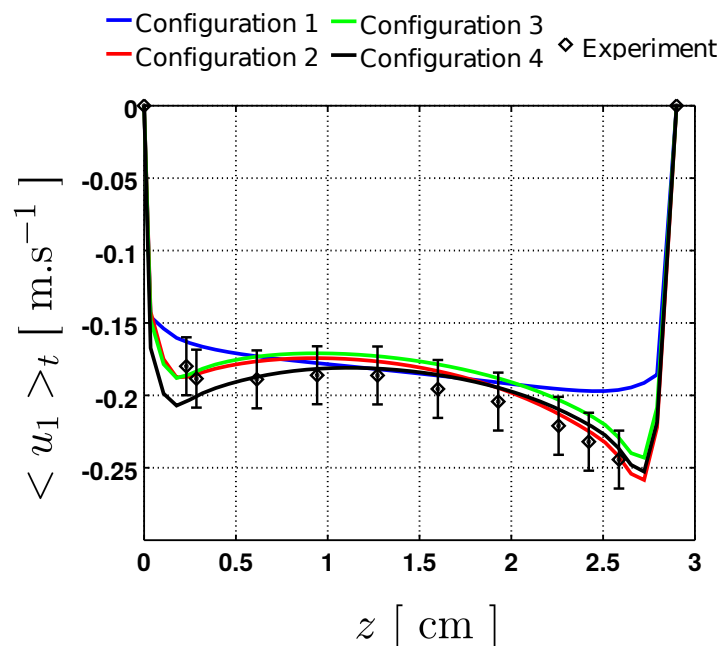

Figure 11: Time averaged flow pattern in the vertical yz-plane ($x = 0.0295$ cm) at the bottom vent for configurations 1 to 4 and experimental PIV data: $< u_1 >_t$ mid-vertical profile ($y = 0$)

The influence of the size of the exterior domain is mainly sensitive at the extremities where the highest absolute values have been recorded. We see that the profile obtained from the experiment takes almost the same profile as those obtained with configurations 2 to 4 where the values remain within the experimental measurement error (0.02 m.s^{-1} absolute error). However, the best results are found

using configuration 4. This is confirmed by looking at the lower region near the injection where we see the similar flow patterns obtained from the simulation of configuration 4 and from the real experiment (figure 12). The time averaged contour lines of the velocity magnitude in the mid xz-plane $(< u_1 >_t^2 + < u_3 >_t^2)^{1/2}$ show great similarities.

Configuration 4   Experiment

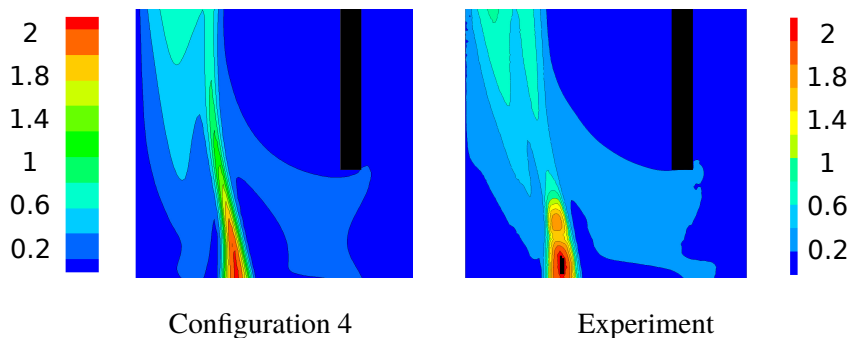Figure 12: Time averaged flow pattern in the vertical xz-plane $(y = 0)$ at the bottom vent for configuration 4 and the experimental PIV data: $(< u_1 >_t^2 + < u_3 >_t^2)^{1/2}$

4   Conclusions and perspectives

The influence of the outlet boundary on an air-helium buoyant jet in a two vented enclosure was studied by LES using the classical Smagorinsky SGS model. Numerical simulations were carried out on four geometrical configurations having the same cell size. Analyses on time averaged quantities show a lot of similarities in the flow pattern for all configurations; basically the kinetic energy distribution and the deformation of the jet axis. However, significant discrepancies have been educed on the helium distribution in the cavity and on the global averaged quantities like volumetric and mass flow-rates. It has been shown that configuration without an exterior domain underestimates the volumetric flow rate of fresh air entering the cavity and thus overestimates the total mass of helium. Comparisons between experimental and numerical simulations in a region near the bottom vent seems satisfactory when taking into account an exterior domain. Further investigations must be undertaken to confirm these primary results.

Mainly, a convergence study on the size of the exterior domain and a qualification of the observed Coanda effect-like remain in our first future perspectives. In a next step, we aim to follow an approach similar to that carried in [19] to define a Robin-type outlet boundary condition that can be applied directly on the surfaces of the vents, without the need of an exterior domain and thus representing correctly the flow inside the cavity.

Further experimental PIV measurements are in progress allowing a more detailed comparison in the whole domain.

Acknowledgements

References

[1] B. Cariteau and I. Tkatschenko , Experimental study of the concentration build-up regimes in an enclosure without ventilation, International Journal of Hydrogen Energy, 37 (22) : 17400 - 17408, 2012.

[2] W. Rodi , Turbulent buoyant jets and plumes, Oxford: Pergamon press, 1982.

[3] W. E. Mell, A. Johnson, K. B. McGrattan and H. R. Baum, Large eddy simulations of buoyant plumes, Chemical and Physical Processes in Combustion, 187 - 190, 1995.

[4] R. Satti, K. Pasumarthi and A. Agrawal, Numerical simulations of buoyancy effects in low density gas jets, In 42nd AIAA Aerospace Sciences Meeting and Exhibit, 1317 - 1327, 2004.

[5] R. Friedrich and W. Rodi, Advances in LES of Complex Flows, Proceedings of the Euromech Colloquium 412, Springer Science & Business Media, 65 : 377, 2002.

[6] G. Blanquart and H. Pitsch, Large-eddy simulation of a turbulent buoyant helium plume, Bulletin of the American Physical Society, 53 : 245 - 252, 2008.

[7] C. J. Chen and W. Rodi, Vertical turbulent buoyant jets: a review of experimental data, NASA STI/Recon Technical Report A, 80,1980.

[8] R. Kalter, M. J. Tummers, J. B. W. Bettink, B. W. Righolt, S. Kenjeres and C. R. Kleijn, Aspect Ratio Effects on Fluid Flow Fluctuations in Rectangular Cavities, Metallurgical and Materials Transactions B, 45 (6) : 2186 - 2193, 2014.

[9] H.L. Tran, Simulation numérique de convection naturelle d'un mélange binaire: cas d'un panache d'hélium en cavité, Ph.D. thesis, Université Pierre et Marie Curie - Paris VI, 2013.

[10] H. N. Najm, P. S. Wyckoff and O. M. Kino, A semi-implicit numerical scheme for reacting flow: I. stiff chemistry, Journal of Computational Physics, 143 (2) : 381 - 402, 1998.

[11] S. Hamimid, M. Guellal and M. Bouafia, Numerical study of natural convection in a square cavity under non-Boussinesq conditions, Thermal Science, (00) : 84 - 84, 2014.

[12] B. Müller, Low mach number asymptotics of the navier-stokes equations and numerical implications, von Karman institute for fluid dynamics, lecture series, 1999.

[13] C. R. Wilke, A viscosity equation for gas mixture, The Journal of Chemical Physics, 18 (4) : 517 - 519, 1950.

[14] M. V. Pham, F. Plourde and K. S. Doan, Direct and large-eddy simulations of a pure thermal plume, Physics of Fluids, 19 (12) : 125103, 2007.

[15] Z. Cheng, V. M. Agranat and A. V. Tchouvelev, Vertical turbulent buoyant helium jet-CFD modeling and validation, In Proceeding of the 1st International Conference on Hydrogen Safety, 2005.

[16] N.R. Panchapakesan and J.L. Lumley, Turbulence measurements in axisymmetric jets of air and helium. Part 2. Helium jet, Journal of Fluid Mechanics, 246 : 225-247, 1993.

[17] CEA TRUST-TrioCFD code, http://www-trio-u.cea.fr

[18] S. Chhabra, P. Huq and A. K. Prasad, Characteristics of small vortices in a turbulent axisymmetric jet, Journal of fluids engineering, 128 (3) : 439 - 445, 2006.

[19] S. Benteboula, Résolution des équations de Navier-Stokes à faible nombre de Mach: Application à l'étude de l'anneau de vorticité à masse volumique variable, Doctoral dissertation, université de Marne-la-Vallée, 2006.